

Heterogeneous Doping *via* Nanoscale Coating Impacts Mechanics of Li Intrusion in Brittle Solid Electrolytes

Xin Xu^{1,4,7†*}, Teng Cui^{2†}, Geoff McConohy^{1,4†}, Harsh D. Jagad^{6†}, Yufei Yang¹, Sunny Wang^{3,4}, Samuel S. Lee², Celeste Melamed¹, Edward Barks^{1,4}, Emma Kaeli¹, Leah Narun¹, Yi Cui¹, Zewen Zhang¹, Hye-Ryoung Lee¹, Rong Xu¹, Melody M. Wang¹, Ajai Romana¹, Alexis Geslin¹, Robert Sinclair¹, Yi Cui^{1,4,5}, Yue Qi^{6*}, X. Wendy Gu^{2*}, William C. Chueh^{1,4,5*}

¹Department of Materials Science and Engineering, Stanford University, Stanford, CA, USA

²Department of Mechanical Engineering, Stanford University, Stanford, CA, USA

³Department of Chemistry, Stanford University, Stanford, CA, USA

⁴Stanford Institute for Materials and Energy Sciences, SLAC National Accelerator Laboratory, Menlo Park, CA, USA

⁵Department of Energy Science and Engineering, Stanford University, Stanford, CA 94305, USA

⁶School of Engineering, Brown University, Providence, RI, USA

⁷Present Address: The Polytechnic School, Ira. A. Fulton Schools of Engineering, Arizona State University; Mesa, AZ 85212, United States.

*Corresponding author emails:

xxu@asu.edu, yueqi@brown.edu, xwgu@stanford.edu, wchueh@stanford.edu

†These authors contributed equally to this work.

Abstract

Lithium metal electroplating and short-circuiting limit fast charging in solid-state batteries, yet the mechanisms and methods to regulate lithium intrusions are not well-understood. In this work, we discover that nanoscale heterogeneous Ag⁺ doping dramatically affects lithium intrusion in Li_{6.6}La₃Zr_{1.6}Ta_{0.4}O₁₂ (LLZO), a brittle solid electrolyte. We generate nanoscale Ag⁺ doping by thermally annealing a 3-nm-thick metallic film. The metallic Ag undergoes Ag-Li ion exchange, completely disappears, and diffuses into LLZO bulk and grain boundaries to a depth of 20-50 nm. Density functional theory calculations predict this Ag-Li ion exchange exhibits negligible impact on electronic properties. Mechanically, nanoindentation experiments ($n = 69$) show a fivefold increase in the force required to fracture Ag⁺ surface-doped LLZO (Ag⁺-LLZO), providing direct evidence that surface modification due to Ag⁺ incorporation prevents crack opening. Conducting 121 plating experiments *via* operando microprobe scanning electron microscopy, we further confirm that the Ag⁺-LLZO surface exhibits improved lithium plating even under a large local indentation stress of 3 GPa. Surprisingly, microprobe plating reveals that Ag⁺ increases the diameter of plated Li at failure by more than 4 times, demonstrating its role in enhancing the defect tolerance of LLZO. Our study reveals a chemo-mechanical mechanism *via* surface heterogeneous doping, complementing the present bulk design rules to prevent mechanical failures in solid-state batteries.

Introduction

Lithium penetration into solid electrolytes (termed Li intrusion) limits charging rate and poses safety concerns in solid-state batteries^{1,2} as well as in electrolysis cells for extracting lithium metal^{3,4} and separating hydrogen isotopes⁵. In brittle garnet solid electrolytes, mechanical imperfection in solid electrolytes is a key cause of Li intrusions, including surface defects such as nanoscale cracks^{6–9} and internal defects such as voids and grain boundaries^{10–15}. Metallic lithium formed during electroplating at these defects builds up stress and propagates cracks once the electrolyte fracture strength is exceeded.^{7–9} Electronic conductivity and trapped electrons at these defects can further promote metallic lithium nucleation and growth inside of the solid electrolyte.^{13–15} Conceptually, three key components contribute to the Li intrusion process: defects, which serve as the active sites for Li intrusion initiation; local current density at these defects, which acts as the driving force for electrochemical stress accumulation; and the solid electrolyte's fracture strength, which determines the critical current density at which an intrusion is initiated.

In brittle solid electrolytes, nanoscale defects (particularly nano-cracks) form easily during processing and handling due to the brittle nature of oxide ceramics, even for high density samples. Specifically, surface cracks can easily result from polishing, uneven applied stack pressure, and impacts. The predominant mitigation strategies have focused on decreasing the local current density during operation through methods such as interlayers and structural modifications.^{16,17} In particular, metallic coatings are effective for regulating Li electroplating in solid-state batteries. Mechanistically, it is believed that metallic coatings improve the contact and wetting of Li metal¹⁸. Among various metals, metallic silver has stood out for enabling fast and

uniform Li electroplating owing to good wettability and decreasing the Li nucleation energy when applied as a coating on solid electrolytes.^{19–21}

Alternatively, methods to enhance material strength and toughness have received recent attention. Residual compressive stress at the surface of solid electrolytes was predicted to prevent Li intrusion^{22,23}. One route to generate such residual compressive stress is physical ion implantation^{24,25}, though this method potentially generates a resistive surface layer that hinders Li ion transport. Thus, there is a critical need to identify a model material system with engineerable compressive stress and to establish a platform for dynamically observing Li intrusion. Among potential routes to generate compressive stress, surface doping is an attractive path. In particular, silver ions exhibit high polarizability and possess a large ionic radius compared to that of lithium ions, suggesting that they may induce significant residual stress when doped into host materials. Such Ag-Li ion exchange has been extensively investigated in many Li containing oxides for optical waveguides and glass-ceramics, using either a molten salt method^{26,27} or a Ag metal electrode^{28,29}. One challenge in this context is the decoupling of the effect of metallic Ag (which improves wetting and enhances electronic contact) from that of Ag-Li ion exchange.

In terms of chemo-mechanical characterization, *operando* microprobe scanning electron microscopy (SEM) has emerged as a powerful platform for investigating electro-chemo-mechanics and local defects in solid-state batteries.^{9,30–34} Operating at the microscale, the microprobe's tip functions as a microscopic electrode/current collector (~1 μm), enabling the exploration of local defects and their impact on the Li electroplating process. This contrasts with conventional Li electroplating using macroscopic electrodes (>>1 mm). Importantly, the

microprobe can generate surface defects *in-situ* *via* controllable mechanical force, rendering it ideal for investigating the effect of mechanically-generated defects on electrochemical reactions.^{35,36} Furthermore, leveraging the high spatial resolution of SEM, this micro-contact approach observes both vertical and lateral growth of Li electroplating at the nanoscale. The latter is particularly important as the contact area determines the current density. Focused-ion beam (FIB) at the same location images the sub-surface microstructure at the Li intrusion site. In this work, we demonstrate Ag⁺ surface doping chemo-mechanically impacts Li intrusion, without contributions from metallic Ag. We surface dope LLZO by thermally annealing a 3-nm metallic Ag thin film. X-ray photoelectron spectroscopy (XPS) depth profiling confirms the incorporation of oxidized Ag⁺; nanoscale secondary ion mass spectrometry (NanoSIMS) depth profiling shows that Ag⁺ diffuses into the subsurface of LLZO by 20-50 nm. Using *operando* microprobe SEM, we carry out 121 local Li electroplating experiments across various locations and sample batches. Ag⁺ surface-doped LLZO (Ag⁺-LLZO) demonstrates enhanced stability during Li electroplating at local current density over 250 mA/cm² even when damaged mechanically by an exceptionally high local stress of 3 GPa (applied *via* the microprobe). Specifically, we observe a 40% increase in mean local critical current density and an expansion of the mean electroplating diameter at failure by over four times compared to uncoated LLZO. We interpret the significant expansion of the plated area at failure as an improved surface defect tolerance attributed to Ag⁺ surface doping (rather than elevated electronic conductivity), enabling a larger current density before failure even in the presence of nanoscale mechanical defects generated by indentation. *In-situ* nanoindentation ($n=69$) quantifies a substantial increase in the loading force necessary to fracture the surface of Ag⁺-LLZO from 5.7 ± 1.5 to 27 ± 3.1 mN

compared to the uncoated LLZO, indicating significant surface toughening. This study demonstrates that nanoscale heterogenous doping is a promising strategy for effectively controlling Li electroplating behavior.

Ag⁺ doping by nanoscale surface coating

We employ a thin film as the metallic silver source to dope the surface of LLZO. To generate a clean and well-defined interface between metallic Ag and LLZO, we cleaved dense LLZO (> 99% of theoretical density) and employed an air-free transfer workflow (Figure 1), rather than the conventional polishing approach.³⁷ First, LLZO was cleaved in an Ar-filled glovebox ($\text{H}_2\text{O} < 0.5\text{ ppm}$, $\text{O}_2 < 0.5 \text{ ppm}$). Then, without air exposure, 1 to 50 nm-thick metallic silver coating was sputtered on the LLZO surface at room temperature (RT) and subsequently annealed between 100 and 400 °C for 1 h (Figure 1a and Figure S1). Cryogenic electron microscopy (Cryo-EM) images validate the pristine interface between metallic Ag and the cleaved LLZO. In contrast, the conventional polishing approach leads to a 10-50 nm-thick contamination layer (Figure S2). Optical images show that LLZO surfaces start to transform from a metallic grey appearance to an amber hue upon annealing a 3-nm metallic Ag coating at 200-300 °C (Figure 1b). This color is consistent with that observed for silver ion incorporation in silicate glass.³⁸

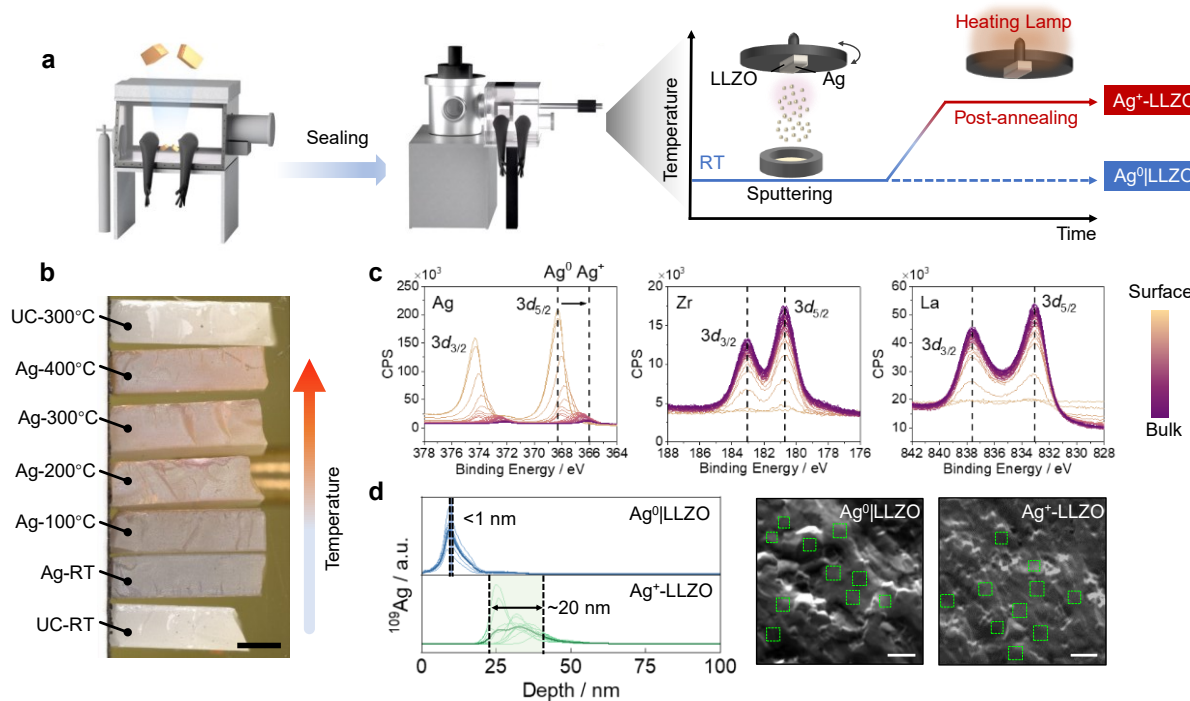


Figure 1. Surface coating on cleaved LLZO with chemical characterization. (a) Pellets are cleaved in an Ar-filled glovebox, transferred to the sputtering chamber integrated with a portable glovebox, and then coated with metallic Ag thin film. This is followed by post-annealing in vacuum (5.0×10^{-7} Torr) at various temperatures. (b) Optical image of uncoated (UC) and 3-nm metallic Ag coated LLZO with post-annealing from room temperature to 400 °C for 1 hour. Scale bar: 2 mm. (c) Depth profiling of valence states of Ag 3d, Zr 3d and La 3d on 20-nm metallic Ag coated LLZO after post-annealing at 300 °C via XPS. Zr is slightly reduced³⁹ with depth during Ar⁺ sputtering process. (d) Depth profiling of ¹⁰⁹Ag isotope on Ag⁰|LLZO (3-nm metallic Ag, without post-annealing) and Ag⁺-LLZO (3-nm metallic Ag, post-annealing at 300 °C) via NanoSIMS. Inset SEM images show locations of measurements. Scale bar: 5 μm.

Next, we examined the valence state of silver near the LLZO surface *via* XPS depth profiling. We first characterized a thick metallic silver layer (20 nm) sputtered on LLZO and post-annealed at 300 °C, providing residual metallic silver which serves as an internal binding energy reference. With depth, the valence state of silver shifts from a metallic Ag⁰ (368.3 eV binding energy) to an oxidized Ag⁺ (366.0 eV) (Figure 1c). In contrast, the Zr 3d and La 3d peak position remain constant (with shifts < 0.1 eV) (see Methods and Figure S3). To confirm that the silver peak shift is not an artifact of Ar sputtering, we performed XPS depth profiling on a 1-μm-thick metallic silver film on silicon substrate; binding energy did not shift with depth (Figure S4). Additionally, XPS on a thin metallic silver coating (3 nm) shows no metallic silver on the LLZO surface after post-annealing at 300 °C (Figure S5), confirming a complete diffusion into LLZO. Finally, the XPS revealed no detectable impurities in the sputtered metallic silver film (Figure S6).

We also analyzed the elemental distribution at the Ag and LLZO interface. Cryo-scanning transmission electron microscopy electron energy loss spectroscopy (Cryo-STEM EELS) mapping suggests silver diffusion into LLZO by approximately 10 nm (Figure S7). To more robustly-quantify the extent of silver diffusion in LLZO, we employed NanoSIMS on the 3-nm metallic Ag coated LLZO, offering elemental sensitivity to the ppm level as well as lateral spatial resolution up to 50 nm (Figure 1d). After post-annealing, Ag is detected at a depth between 20 and 50 nm in LLZO with an average peak position at a depth of 28 nm. The Ag depth profiling varies substantially as a function of lateral position, likely due to grain-to-grain variation of silver diffusion. Additionally, a surface Li-enriched layer is observed on the annealed sample (Figure S8). In contrast, Ag is detected only at depths less than 20 nm on the non-annealed sample (corresponding to the metallic Ag film), with all samples yielding silver peak (maximum

Ag counts) splitting within a tight 1 nm window (additional NanoSIMS data are shown in Figure S9). The profile broadening observed on the non-annealed sample could be attributed to the finite probe size and atomic mixing resulting from primary ion bombardment.^{40,41} We hypothesize that the large profile broadening (with respect to lateral position) on the annealed sample is due to a variation of silver diffusion rates in LLZO grains of different crystallographic orientations, possibly due to diffusion along the grain boundary (Figure S10). Indeed, we observe silver segregation at grain boundaries to an average depth of 33 nm (Figure S11). We note that the actual depth of silver diffusion may exceed this, as silver segregation to grain boundaries at greater depths could be beyond the detection limit of NanoSIMS. Together, optical microscopy, XPS and NanoSIMS depth profiling confirm the diffusion of Ag⁺ in LLZO after post-annealing metallic Ag thin films. Hereafter, we will use the term “Ag⁺-LLZO” to denote Ag⁺ doped LLZO, obtained by annealing 3-nm metallic Ag on LLZO at 300 °C, and “Ag⁰|LLZO” to denote LLZO coated with metallic Ag without annealing.

Mechanism of Ag⁺ doping in LLZO

We carry out DFT calculations to understand the Ag⁺ doping mechanism. The defect formation energy (E_f) of ion exchanging Li⁺ with Ag⁺ in the pristine LLZO was computed as per the methods section. In the ion exchange reaction $Li_{Li} + Ag_{surface} \rightarrow Ag_{Li}^X + Li_{surface}$ (Kröger–Vink notation) where metallic Ag is the reactant and metallic Li as the product, the E_f is ~3.7 eV, which is prohibitively high. Yet, the presence of trace impurities can lower the defect formation energy significantly, specifically oxygen. In an oxidizing environment, the ion exchange reaction becomes $Li_{Li} + Ag_{surface} + \frac{1}{4}O_2 \rightarrow Ag_{Li}^X + \frac{1}{2}Li_2O_{surface}$. For this reaction,

we compute an E_f of ~ 0.92 eV (with respect to O₂ molecule). This significantly lowered E_f is due to the formation of stable Li₂O rather than metallic Li, and indicates that the Ag-Li ion exchange is possible, especially at elevated temperatures. The computationally predicted Ag-Li ion exchange is consistent with experimental observations that lithium in some form segregates to the LLZO surface after Ag⁺ doping (Figure S8) and precipitate as a second phase (Figure S12).

We also use DFT calculations to explore the electronic properties of Ag⁺-LLZO. The lowest energy configuration for the Ag-Li ion exchange in LLZO occurs when a Ag⁺ replaces a Li⁺ on the slightly larger octahedral Li⁺ (96h) site (Figure 2a). The electronic partial density of states (pDoS) was compared to that of pristine LLZO. In Figure 2c-d, 2f-g, the atoms in Ag⁺-LLZO are shown in dotted lines, while the corresponding atoms for the pristine LLZO are shown in solid lines. Specifically, the atomic density of states for the oxygen neighboring the silver in Ag⁺-LLZO are shown in Figure 2e and the non-neighboring oxygen are shown in Figure 2f. We first note that the energetic difference between the valence band maximum (VBM) and the conduction band minimum (CBM) for the pristine LLZO case is ~ 4.2 eV, consistent with literature reports⁴². It is evident that the Li, La, Zr and non-neighboring O pDoS and the electronic bandgap for the pristine and the Ag⁺-LLZO remains unchanged.

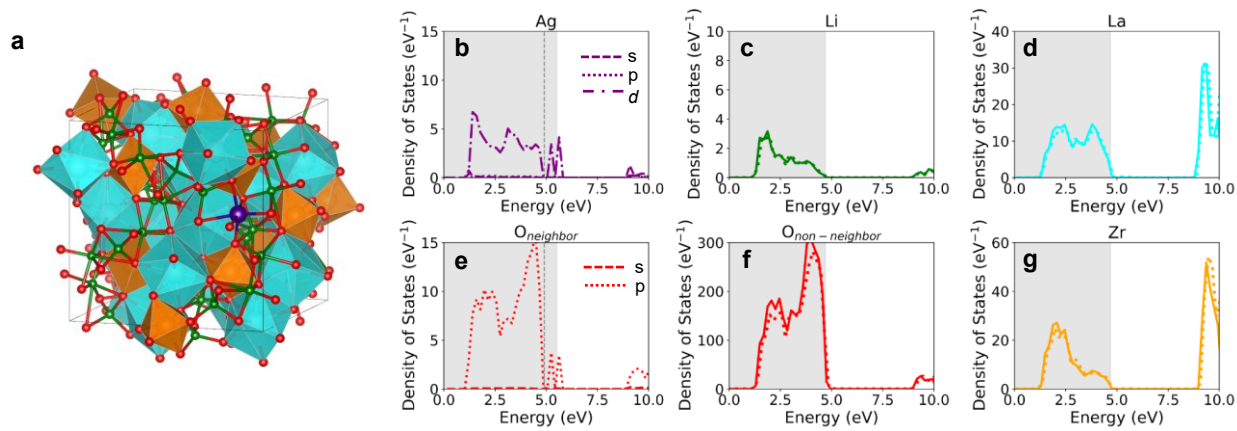


Figure 2: Comparison of the electronic partial density of states occupation between uncoated pristine LLZO (solid lines) and Ag^+ -LLZO (dotted lines). (a) Schematic for Ag^+ -LLZO. Cyan and orange polyhedral for La and Zr respectively, green lines for Li and purple lines for Ag. (b) The orbital resolved partial density of states occupation of the Ag showing major contribution from d orbital. Dotted gray lines represent the valence band maximum from c-d, and f-g. (c) The partial density of states occupation of the Li. (d) The partial density of states occupation of the La. (e) The orbital resolved partial density of states occupation of the neighboring O to Ag in Ag^+ -LLZO showing major contribution from p orbital. Dotted gray lines represent the valence band maximum from c-d, and f-g. (f) The partial density of states occupation of the non-neighboring O. (g) The partial density of states occupation of the Zr. The Gray region signifies occupied states.

The orbital-resolved pDoS of the silver and its local oxygen neighbors for the Ag^+ -LLZO are shown in Figure 2b and Figure 2e, respectively. The dotted gray line represents the VBM of the pristine case shown in Figure 2c-d, f-g. An interesting contribution close to the VBM is observed. This contribution is due to the O-p and Ag-d orbitals, thus introducing defect states close to the

VBM. These are isolated defect states that are locally bound to the silver. Additionally, the charge state of the silver ion is predicted to be lower than that of lithium ion, indicating Ag-O bonds are more covalent than Li-O bonds (see the charge state discussion in SI).

Lithium electroplating *via* microprobe

To quantify the electrochemical properties of Ag^+ -LLZO generated by annealing a 3-nm-thick metallic thin film between 100 and 400 °C, we perform *operando* Li electroplating using an electrical microprobe platform inside FIB/SEM^{9,30} (Figure 3a-c). We further utilize the microprobe to indent the LLZO surface to mechanically generate defects, and carry out cryo-EM to image the indentation site while minimizing beam-induced damage. In the pristine, unindented LLZO, we observed no pre-existing nanoscale cracks up to a depth of 100 nm across a 10 μm wide FIB-prepared LLZO lamella (Figure 3d). To simulate mechanical damage, we apply a large local stress of 3 GPa by indenting a microprobe onto the LLZO surface. We observe nanoscale cracks < 2 nm in width at depths up to ~ 20 nm (Figure 3e, sample preparation detailed in Figure S13 and additional cryo-EM data shown in Figure S14).

During linear sweep voltammetry inside the SEM, we measure two important aspects of Li electroplating: the diameter of plated Li and the critical current density at the onset of Li intrusion. The diameter of plated lithium is controlled by factors including surface Li wetting, defect density, and surface electronic transport. The latter is especially important considering that we deposit metallic silver prior to thermal annealing, a point that we return to later. We note that the lithium plating diameter was directly observed through SEM images rather than being

inferred based on the electrochemical constriction models in our previous study.⁹ (see discussion in Figure S15).

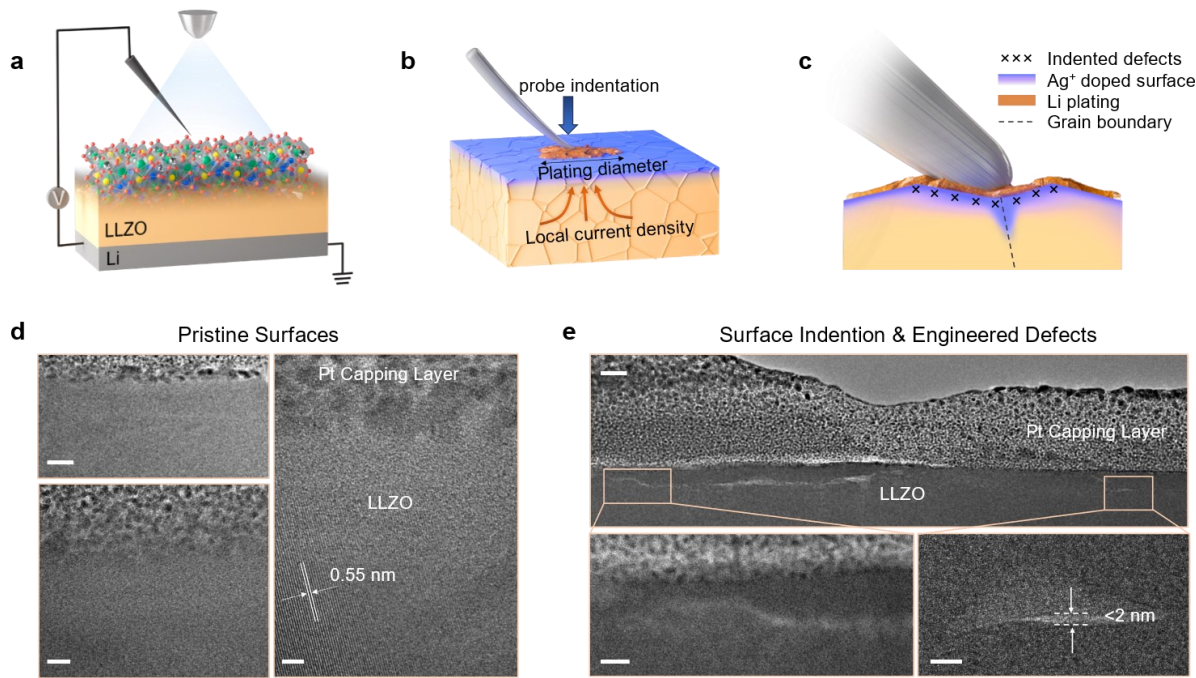


Figure 3. Operando Li electroplating and local defects engineering via microprobe experiments inside the SEM. (a) Schematics of *operando* microprobe experiments inside the SEM. (b) Schematics of local plating, plating diameter and local current density. (c) *In-situ* generation of local defects using a microprobe followed by subsequent local plating in the nearby vicinity. (d) Cryo-EM images of uncoated pristine LLZO surface without noticeable nanoscale cracks up to a depth of 100 nm. Scale bars: left-top 20 nm, left-bottom 10 nm, and right 5 nm. (e) Cryo-EM images of LLZO surfaces show nano-cracks within a depth of 20 nm after a large indentation stress of 3 GPa. Scale bars: top 30 nm, left-bottom 10 nm, left-right 5 nm.

Exemplary *operando* SEM results show that even under a large indentation stress of 3 GPa, Ag⁺-LLZO (annealed at 300 °C) gives uniform lithium plating over a larger area before short circuit compared to both uncoated LLZO and Ag⁰|LLZO (without post-annealing) (Figure 4a). A comprehensive statistical analysis was conducted by measuring the final lithium plating diameter and local current density at failure across 121 different locations of various samples in Figure 4b. The plotting of local critical current density against plating area here is inspired by the field of failure mechanics, where the plating area reflects both the density of surface defects as well as the tendency of these defects to nucleate Li intrusion.

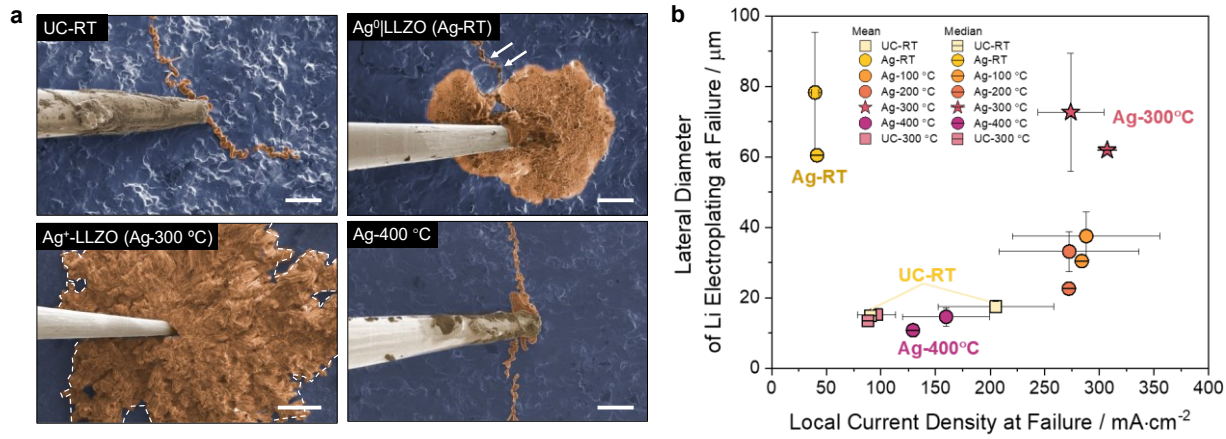


Figure 4. Improved Li electroplating stability *via* Ag⁺ doping. (a) Colorized SEM images of Li electroplating on uncoated (UC) and 3-nm metallic Ag coated LLZO at various post-annealing temperatures under a local stress of 3 GPa. Here, Ag-RT corresponds to Ag⁰|LLZO, and Ag-300 °C corresponds to Ag⁺-LLZO as denoted above. Scale bars: 10 μm for UC-RT, Ag-RT, Ag-400 °C, and 50 μm for Ag-300 °C. (b) The lithium plating diameter and local current density at failure for uncoated LLZO ($n = 43$ for RT, $n = 13$ for 300 °C), and 3-nm metallic Ag coated

LLZO at various post-annealing temperatures ($n = 17$ for RT, $n = 12$ for $100\text{ }^{\circ}\text{C}$ - $400\text{ }^{\circ}\text{C}$) under a local stress of 3 GPa. The lithium plating diameter is calculated as $d = \sqrt{4A/\pi}$ where A is the lithium plating area.

Surprisingly, while the Ag^+ -LLZO shows a slightly improved local critical current density relative to uncoated LLZO (from 200 ± 50 to $280 \pm 30\text{ mA/cm}^2$), the plating area at failure is much larger with Ag^+ surface doping (from 17 ± 1.5 to $73 \pm 17\text{ }\mu\text{m}$). As demonstrated in previous work⁹, local critical current density in microprobe experiments is orders of magnitude greater than in macroscopic cells because the Li intrusion is controlled by the defect density rather than solely by the rate of plating.

As mentioned, both the local critical current density and plating diameter depend strongly on the annealing temperature. Among the annealing conditions, Ag^+ -LLZO annealed at $300\text{ }^{\circ}\text{C}$ exhibit the largest plating diameter at failure (Figure 4b). For example, Ag^+ -LLZO annealed at $400\text{ }^{\circ}\text{C}$ shows a substantial decrease in both plating diameter and critical current density compared to those annealed at $300\text{ }^{\circ}\text{C}$. This is likely due to surface lithium loss^{43,44} at elevated temperatures which could induce tensile stress to the LLZO surface. Alternatively, the higher temperature may facilitate deeper silver diffusion, resulting in a lower concentration of Ag^+ near the surface. Following previous work, we also performed a Weibull analysis to quantify the relationship between the failure probability and the total amount of plated Li for each annealing condition (Figure S16), further confirming the strong dependence of failure probability on annealing temperature.

For completeness, we also examined the local critical current density of LLZO with metallic Ag coating, obtained without thermal annealing. Although $\text{Ag}^0|\text{LLZO}$ shows comparable mean plating area to the $\text{Ag}^+|\text{LLZO}$ surface due to the high electronic conductivity of metallic Ag (effectively expanding the probe contact area), both the mean critical local current density and the total amount of plated Li are significantly decreased (Figure S17). We note that the primary factor hindering the uniform plating of Li over the entire surface of $\text{Ag}^0|\text{LLZO}$ is the high sheet resistance of the thin 3-nm Ag coating.

One plausible explanation for the increased plating area in Ag^+ surface-doped LLZO is an increase in the surface electronic conductivity due to the Ag^+ doping (i.e., Ag^+ doping is electronically compensated by Zr^{4+} reduction⁴⁵). Nonetheless, DFT calculations suggest that Ag^+ only introduces isolated state and is not expected to significantly alter the electronic conductivity. To corroborate this experimentally, we qualitatively infer surface electronic conductivity from the lithium plating diameter *via operando* microprobe SEM. Specifically, we compared the lithium plating diameter at failure between uncoated LLZO, $\text{Ag}^+|\text{LLZO}$ and $\text{Ag}^0|\text{LLZO}$ (Figure 5). Multiple independent tests ($n = 29$ for uncoated LLZO, $n = 13$ for $\text{Ag}^+|\text{LLZO}$, $n = 15$ for $\text{Ag}^0|\text{LLZO}$) were performed a low indentation stress arising from the microprobe (<100 MPa) to minimize the impact of external stress on surface conductivity. If the $\text{Ag}^+|\text{LLZO}$ samples exhibited an increase in surface electronic conductivity, we would expect that the aspect ratio of Li electroplating would be larger than uncoated LLZO due to facile lateral charge transport. The lateral diameter was measured based on the SEM images while the height of the plated Li was estimated by dividing the total plated Li volume (converted from total lithium plating capacity) by the plating area.

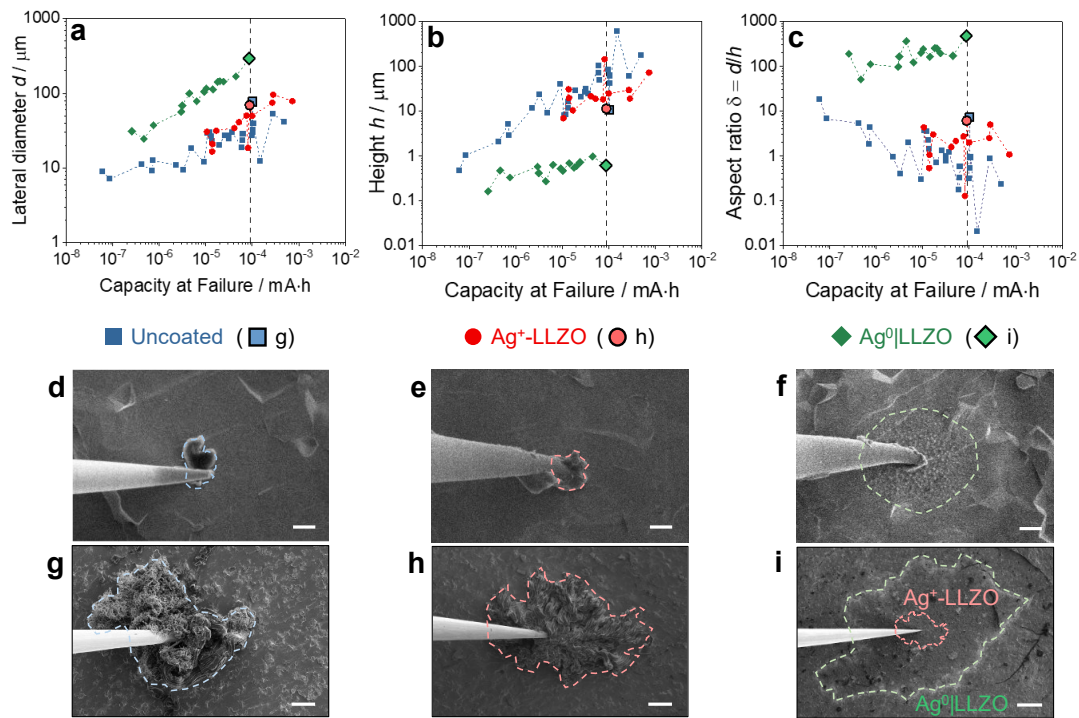


Figure 5. Lateral and vertical growth of local Li electroplating on LLZO under minimal local stress (<100 MPa) via *operando* SEM experiments. (a) The measured lateral plating diameter d , (b) the calculated height h , and (c) the aspect ratio $\delta = d/h$ of Li electroplating at failure on the uncoated ($n = 29$), Ag^+ -LLZO ($n = 13$), and $\text{Ag}^0|\text{LLZO}$ surfaces ($n = 15$); Exemplary SEM images of the initial Li electroplating on (d) uncoated, (e) Ag^+ -LLZO, and (f) $\text{Ag}^0|\text{LLZO}$ surfaces with initial plating capacity of $1.2 \times 10^{-9} \text{ mA} \cdot \text{h}$. Exemplary SEM images of the final Li electroplating at failure on (g) uncoated, (h) Ag^+ -LLZO, and (i) $\text{Ag}^0|\text{LLZO}$ surfaces with terminating plating capacity of $9.0 \times 10^{-5} \text{ mA} \cdot \text{h}$. The local Li electroplating regions are highlighted in colored dashed lines. (d) and (g) are of the same experiment, (e) and (h) are of the same experiment, and (f) and (i) are of the same experiment. (g-i) are indicated on (a-c). All Ag

coating thickness before post-annealing is 3 nm. Scale bars, Figure (d-f): 1 μm . Figure (g-h): 15 μm , and Figure (i): 50 μm .

Experimentally, the aspect ratio of electroplated Li at different failure capacities reveals no substantial differences between uncoated and Ag^+ -LLZO surfaces (Figure 5a-c). This indicates that Ag^+ doping has no substantial impact on the surface electronic conductivity. In contrast (and as would be expected), $\text{Ag}^0|\text{LLZO}$ exhibits a significantly larger aspect ratio, suggesting predominantly lateral Li growth during electroplating. This is expected due to the high conductivity of metallic Ag before it has incorporated as a dopant during annealing. The similarity in the aspect ratio of plated Li between uncoated and Ag^+ -LLZO also suggests that the surface doping does not substantially modify Li wetting, unlike in the case of metallic Ag coating.

To make the analysis quantitative, we compared the aspect ratio of plated Li across different samples at the same terminating lithium plating capacity at failure ($9.0 \times 10^{-5} \text{ mA}\cdot\text{h}$). In Figure 5d-f, SEM imaging at the initial plating capacity ($1.2 \times 10^{-9} \text{ mA}\cdot\text{h}$), corresponding to 0.0013 % of the terminating capacity, reveals identical Li nucleation morphology for the uncoated and Ag^+ -LLZO (a lithium deposit of $\sim 1.5 \mu\text{m}$ plating diameter) near the microprobe tip. In contrast, the Li nucleation morphology on the metallic $\text{Ag}^0|\text{LLZO}$ reveal multiple (apparently disconnected) small granular lithium deposits spreading within an area of $\sim 5 \mu\text{m}$ plating diameter. The lithium morphology at the same terminating capacity further emphasizes the difference in plating area (Figure 5g-i): uncoated and Ag^+ -LLZO has a lateral plating diameter of $\sim 70 \mu\text{m}$, while the

$\text{Ag}^0|\text{LLZO}$ has a lateral plating diameter of 290 μm . This result is consistent with prior work that metallic Ag^0 coating improves wettability through the formation of Li-Ag alloy^{19–21}. Despite the improved wettability, short circuit events still occur at a lower plating capacity for $\text{Ag}^0|\text{LLZO}$ (the mean terminating capacity of $1.6 \times 10^{-5} \text{ mA}\cdot\text{h}$) compared to that of $\text{Ag}^+|\text{LLZO}$ (the mean terminating capacity of $1.4 \times 10^{-4} \text{ mA}\cdot\text{h}$) (Figure 5 and Figure S16).

Surface compressive stress *via* Ag^+ doping

To understand the origin of substantially expanded plating diameter at failure, surface mechanical properties were evaluated using a nanoindenter under vacuum inside an SEM (Figure 6). A cube corner tip was intentionally employed to accelerate the onset of surface cracks with loading force kept to a maximum of 50 mN (Figure 6a-b). A total of $n = 29$ baseline experiments were performed on uncoated LLZO while $n = 40$ experiments were performed on $\text{Ag}^+|\text{LLZO}$. The LLZO sample for each surface condition came from two different batches to decrease statistical bias from individual sample variations. Figure 6c-d features a Hertzian contact stress curve observed on the leftmost side of all measured loading-depth curves, indicating surface fractures occurring during the loading process (see Methods). This observation is consistent with SEM imaging findings presented in Figure S18. The loading force at initial crack formation for all $n = 69$ experiments is summarized in the histogram depicted in Figure 6e (additional histograms for different batches in Figure S19). A notable difference in the histogram is apparent within the range of 0–5 mN, with initial fractured depths spanning 0–500 nm. The data indicates that the mean initial force necessary to fracture $\text{Ag}^+|\text{LLZO}$ is substantially larger ($27 \pm 3.1 \text{ mN}$) than uncoated LLZO ($5.7 \pm 1.5 \text{ mN}$). We note that 11 out of 44 indentations on $\text{Ag}^+|\text{LLZO}$ do

not show any fracture behavior before reaching the maximum force of 50 mN. Therefore, a value of 50 mN is used for each non-fractured case when calculating the mean force.

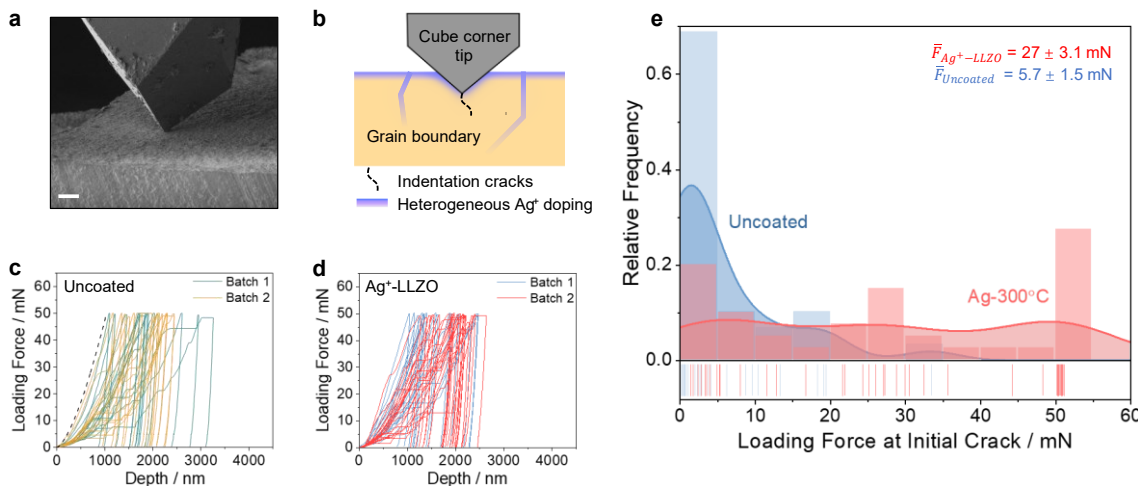


Figure 6. Mechanical characterization of Ag^+ -LLZO surfaces via *in-situ* nanoindentation (3-nm metallic Ag, post-annealing at 300 °C). (a) SEM image of the *in-situ* nanoindentation with a cube corner tip. Scale bar: 50 μm. (b) Schematics of surface toughening mechanism due to Ag^+ doped surface and grain boundaries. (c) Loading-depth curves of uncoated LLZO with a total of n = 29 tests with the dashed-line for Hertzian contact stress curve. (d) Loading-depth curves of Ag^+ -LLZO with a total of n = 40 tests. All the samples came from two different batches for reliability. (e) Histogram of the loading force at the initial crack for uncoated and Ag^+ -LLZO surfaces acquired by *in-situ* SEM nanoindentation experiments using a cube corner tip.

Finally, we consider various surface toughening mechanism. Ag-Li ion exchange introduces compressive stress in the nanosized ion-exchange zone due to ionic radius misfit. The concept of surface compressive stress has been experimentally demonstrated for toughening glasses⁴⁶.

Furthermore, silver ions are observed to segregate at LLZO grain boundaries (Figure S11), potentially enhancing the grain boundary fracture toughness. The surface toughening will prevent cracks opening resulting from lithium intrusion, and therefore improve the stability of Li electroplating. Although how the nanoscale surface Ag^+ modification manifested to the microscale fracture behavior still requires further investigation, our results demonstrate that annealing ultra-thin Ag coating (3 nm) mitigating crack opening.

Conclusion

In summary, we report a chemo-mechanical approach to decrease failure probability in brittle garnet solid electrolytes by annealing 3-nm Ag coating. Depth profiling indicates the complete incorporation of Ag^+ into the LLZO subsurface via Ag-Li ion exchange, consistent with thermotical predictions. The Ag^+ -LLZO surface exhibits enhanced tolerance against Li intrusion compared to the uncoated LLZO, as evidenced by improved local current density and expanded electroplating area. Nanoindentation experiments reveal a substantial surface toughening that accompanies Ag^+ doping into LLZO, taking place both in the bulk and along grain boundaries. Our study highlights the viability of nanoscale heterogenous doping strategy for decreasing Li intrusion probability and mitigating short-circuiting in brittle solid electrolytes.

References

1. Cao, D. *et al.* Lithium Dendrite in All-Solid-State Batteries: Growth Mechanisms, Suppression Strategies, and Characterizations. *Matter* **3**, 57–94 (2020).
2. Janek, J. & Zeier, W. G. Challenges in speeding up solid-state battery development. *Nat. Energy* **8**, 230–240 (2023).
3. Zhang, H., Ren, Y., Wu, X. & Wang, N. An interface-modified solid-state electrochemical device for lithium extraction from seawater. *J. Power Sources* **482**, 228938 (2021).
4. Xiong, Y. *et al.* Electrochemical lithium extraction from aqueous sources. *Matter* **5**, 1760–1791 (2022).
5. Teprovich, J. A. *et al.* Electrochemical extraction of hydrogen isotopes from Li/LiT mixtures. *Fusion Eng. Des.* **139**, 1–6 (2019).
6. Tsai, C.-L. *et al.* Li₇La₃Zr₂O₁₂ Interface Modification for Li Dendrite Prevention. *ACS Appl. Mater. Interfaces* **8**, 10617–10626 (2016).
7. Porz, L. *et al.* Mechanism of Lithium Metal Penetration through Inorganic Solid Electrolytes. *Adv. Energy Mater.* **7**, 1701003 (2017).
8. Ning, Z. *et al.* Dendrite initiation and propagation in lithium metal solid-state batteries. *Nature* **618**, 287–293 (2023).
9. McConohy, G. *et al.* Mechanical regulation of lithium intrusion probability in garnet solid electrolytes. *Nat. Energy* **1–10** (2023) doi:10.1038/s41560-022-01186-4.
10. Cheng, E. J., Sharafi, A. & Sakamoto, J. Intergranular Li metal propagation through polycrystalline Li_{6.25}Al_{0.25}La₃Zr₂O₁₂ ceramic electrolyte. *Electrochimica Acta* **223**, 85–91 (2017).

11. Shen, F., Dixit, M. B., Xiao, X. & Hatzell, K. B. Effect of Pore Connectivity on Li Dendrite Propagation within LLZO Electrolytes Observed with Synchrotron X-ray Tomography. *ACS Energy Lett.* **3**, 1056–1061 (2018).
12. Tian, H.-K., Xu, B. & Qi, Y. Computational study of lithium nucleation tendency in Li₇La₃Zr₂O₁₂ (LLZO) and rational design of interlayer materials to prevent lithium dendrites. *J. Power Sources* **392**, 79–86 (2018).
13. Han, F. *et al.* High electronic conductivity as the origin of lithium dendrite formation within solid electrolytes. *Nat. Energy* **4**, 187–196 (2019).
14. Tian, H.-K., Liu, Z., Ji, Y., Chen, L.-Q. & Qi, Y. Interfacial Electronic Properties Dictate Li Dendrite Growth in Solid Electrolytes. *Chem. Mater.* **31**, 7351–7359 (2019).
15. Liu, X. *et al.* Local electronic structure variation resulting in Li ‘filament’ formation within solid electrolytes. *Nat. Mater.* 1–6 (2021) doi:10.1038/s41563-021-01019-x.
16. Xiao, Y. *et al.* Understanding interface stability in solid-state batteries. *Nat. Rev. Mater.* **5**, 105–126 (2020).
17. Alexander, G. V., Shi, C., O'Neill, J. & Wachsman, E. D. Extreme lithium-metal cycling enabled by a mixed ion- and electron-conducting garnet three-dimensional architecture. *Nat. Mater.* **22**, 1136–1143 (2023).
18. Dai, J., Yang, C., Wang, C., Pastel, G. & Hu, L. Interface Engineering for Garnet-Based Solid-State Lithium-Metal Batteries: Materials, Structures, and Characterization. *Adv. Mater.* **30**, 1802068 (2018).
19. Feng, W., Dong, X., Li, P., Wang, Y. & Xia, Y. Interfacial modification of Li/Garnet electrolyte by a lithiophilic and breathing interlayer. *J. Power Sources* **419**, 91–98 (2019).

20. Kim, S. *et al.* The Role of Interlayer Chemistry in Li-Metal Growth through a Garnet-Type Solid Electrolyte. *Adv. Energy Mater.* **10**, 1903993 (2020).
21. Xiang, X. *et al.* Improving the Interfacial Contact between Li₇La₃Zr₂O₁₂ and Lithium Anode by Depositing a Film of Silver. *J. Electrochem. Soc.* (2021) doi:10.1149/1945-7111/ac0654.
22. Qi, Y., Ban, C. & Harris, S. J. A New General Paradigm for Understanding and Preventing Li Metal Penetration through Solid Electrolytes. *Joule* (2020) doi:10.1016/j.joule.2020.10.009.
23. Jagad, H. D., Harris, S. J., Sheldon, B. W. & Qi, Y. Tradeoff between the Ion Exchange-Induced Residual Stress and Ion Transport in Solid Electrolytes. *Chem. Mater.* **34**, 8694–8704 (2022).
24. Yao, X. *et al.* Xenon Ion Implantation Induced Surface Compressive Stress for Preventing Dendrite Penetration in Solid-State Electrolytes. *Small* **18**, 2108124 (2022).
25. Flatscher, F. *et al.* Deflecting Dendrites by Introducing Compressive Stress in Li₇La₃Zr₂O₁₂ Using Ion Implantation. *Small* **n/a**, 2307515.
26. Garfinkel, H. M. Ion-exchange equilibria between glass and molten salts. *J. Phys. Chem.* **72**, 4175–4181 (1968).
27. Shah, M. L. Optical waveguides in LiNbO₃ by ion exchange technique. *Appl. Phys. Lett.* **26**, 652–653 (1975).
28. Biesuz, M. *et al.* Solid-state field-assisted ion exchange of Ag in lithium aluminum silicate glass-ceramics: *A superfast processing route toward stronger materials with antimicrobial properties*. *J. Eur. Ceram. Soc.* **42**, 1750–1761 (2022).

29. Ohtsuki, T., Peyghambarian, N., Honkanen, S. & Najafi, S. I. Gain characteristics of a high concentration Er³⁺-doped phosphate glass waveguide. *J. Appl. Phys.* **78**, 3617–3621 (1995).
30. Krauskopf, T. *et al.* The Fast Charge Transfer Kinetics of the Lithium Metal Anode on the Garnet-Type Solid Electrolyte Li_{6.25}Al_{0.25}La₃Zr₂O₁₂. *Adv. Energy Mater.* **10**, 2000945 (2020).
31. Zhao, J. *et al.* In situ Observation of Li Deposition-Induced Cracking in Garnet Solid Electrolytes. *ENERGY Environ. Mater.* **n/a**,
32. Cui, C. *et al.* Unlocking the in situ Li plating dynamics and evolution mediated by diverse metallic substrates in all-solid-state batteries. *Sci. Adv.* **8**, eadd2000 (2022).
33. Wei, Z. *et al.* In Situ Observation of Room-Temperature Magnesium Metal Deposition on a NASICON/IL Hybrid Solid Electrolyte. *Adv. Energy Mater.* **13**, 2302525 (2023).
34. Initiation of Dendritic Failure of LLZO via Sub-Surface Lithium Deposition.
<https://www.researchsquare.com> (2023) doi:10.21203/rs.3.rs-3223027/v1.
35. Kondo, S., Mitsuma, T., Shibata, N. & Ikuhara, Y. Direct observation of individual dislocation interaction processes with grain boundaries. *Sci. Adv.* **2**, e1501926 (2016).
36. Kondo, S., Ishihara, A., Tochigi, E., Shibata, N. & Ikuhara, Y. Direct observation of atomic-scale fracture path within ceramic grain boundary core. *Nat. Commun.* **10**, 2112 (2019).
37. Alam, T. & Das, A. Review on Impurity and Conductivity Issues of Garnet Type Li₇La₃Zr₂O₁₂: Mechanisms, Solutions, and Perspectives. *Energy Fuels* **37**, 15267–15282 (2023).

38. Jiang, X. *et al.* Effect of potassium and silver ion-exchange on the strengthening effect and properties of aluminosilicate glass. *Ceram. Int.* **49**, 31351–31363 (2023).
39. Zhu, Y. *et al.* Dopant-Dependent Stability of Garnet Solid Electrolyte Interfaces with Lithium Metal. *Adv. Energy Mater.* **9**, 1803440 (2019).
40. Andersen, H. H. The depth resolution of sputter profiling. *Appl. Phys.* 131–140 (1979).
41. Zalm, P. C. Ultra shallow doping profiling with SIMS. *Rep. Prog. Phys.* **58**, 1321–1374 (1995).
42. Fabrication and Characterization of Li₇La₃Zr₂O₁₂ Thin Films for Lithium Ion Battery - IOPscience. https://iopscience-iop.org.ezproxy1.lib.asu.edu/article/10.1149/2.013206ssl/meta?casa_token=5_zCSABliJAAAAAA:A:A1_TCSmuVxcFnL83XOrAz9-g4-6hvIYEXNdFJqFXlhOw7s_WnNidp4tQnQ8v1jHhiau8JTUKYQANfq2Jc2w6LzXpXqMe
43. Paolella, A. *et al.* Discovering the Influence of Lithium Loss on Garnet Li₇La₃Zr₂O₁₂ Electrolyte Phase Stability. *ACS Appl. Energy Mater.* **3**, 3415–3424 (2020).
44. Huang, X. *et al.* Developing Preparation Craft Platform for Solid Electrolytes Containing Volatile Components: Experimental Study of Competition between Lithium Loss and Densification in Li₇La₃Zr₂O₁₂. *ACS Appl. Mater. Interfaces* **14**, 33340–33354 (2022).
45. Burrell, M. C. & Gillman, E. XPS investigation of monoatomic and cluster argon sputtering of zirconium dioxide. *J. Vac. Sci. Technol. A* **41**, 043202 (2023).
46. Hale, D. K. Strengthening of Silicate Glasses by Ion Exchange. *Nature* **217**, 1115–1118 (1968).

47. Yu, S. *et al.* Elastic Properties of the Solid Electrolyte Li₇La₃Zr₂O₁₂ (LLZO). *Chem. Mater.* **28**, 197–206 (2016).
48. O’Callaghan, M. P. & Cussen, E. J. Lithium dimer formation in the Li-conducting garnets Li_{5+x}Ba_xLa_{3-x}Ta₂O₁₂ ($0 < x \leq 1.6$). *Chem Commun* 2048–2050 (2007) doi:10.1039/B700369B.
49. Xie, H., Alonso, J. A., Li, Y., Fernández-Díaz, M. T. & Goodenough, J. B. Lithium Distribution in Aluminum-Free Cubic Li₇La₃Zr₂O₁₂. *Chem. Mater.* **23**, 3587–3589 (2011).
50. Jain, A. *et al.* Commentary: The Materials Project: A materials genome approach to accelerating materials innovation. *APL Mater.* **1**, 011002 (2013).
51. Kresse, G. & Hafner, J. Ab initio molecular dynamics for liquid metals. *Phys. Rev. B* **47**, 558–561 (1993).
52. Perdew, J. P., Burke, K. & Ernzerhof, M. Generalized Gradient Approximation Made Simple. *Phys. Rev. Lett.* **77**, 3865–3868 (1996).
53. Das, T., D. Nicholas, J. & Qi, Y. Long-range charge transfer and oxygen vacancy interactions in strontium ferrite. *J. Mater. Chem. A* **5**, 4493–4506 (2017).

Acknowledgements

This work was supported by the Assistant Secretary for Energy Efficiency, Vehicle Technologies Office of the US Department of Energy under the Advanced Battery Materials Research Program. Additional support was provided by Samsung Advanced Institute of Technology. T.C. and X.W.G. acknowledge financial support from StorageX Initiative at Stanford University. Y.C.

acknowledges cryo-EM support from the US Department of Energy, Office of Basic Energy Sciences, Division of Materials Science and Engineering under contract DE-AC02-76SF00515. Acknowledgments are extended to Professor William D. Nix for his invaluable contributions, including insightful discussions and the examination of nanoindentation data and mechanical analyses throughout this study. Additionally, we thank Richard Chin, Juliet Jamtgaard, Paul Wallace, Christine Jilly-Rehak, and Matthew Mills for assistance with Helios SEM/FIB and NanoSIMS. We also thank Lincoln Miara and Srinath Chakravarthy, Stephen J. Harris, Andrew Lee, Yin Liu, James A. Greer for helpful discussions. We extend special thanks to Chaoyang Zhao for his valuable contribution to the art design of the schematics used in this work. Finally, we thank Joon Hyung Lee for helpful discussions and comments on the manuscript. Part of this work was performed at the Stanford Nano Shared Facilities (SNSF), supported by the National Science Foundation under award ECCS-2026822.

Author contributions

X.X., T.C., and G.M. performed most of the experiments and their analysis. Y.Y and S.W. provided XPS analysis. Y.C., Z.Z., H.L., R.S and Y.C. contributed to TEM characterization and analysis. S.L., M.W., and R.X. contributed to the nanoindentation measurements. E.B. contributed to LLZO sample preparation. E.K., L.N., A.R., and A.G. contributed to electrical measurement and data analysis. C.M. contributed to surface coating. H.J. and Y.Q. performed DFT calculation on Ag-Li ion exchange process as well as mechanical stress analysis. X.W.G. supervised the nanoindentation measurement and analysis. X.X. and W.C.C. designed the research plan and supervised the work. X.X. wrote the manuscript with input from all authors.

Data Availability

All relevant data is contained in the manuscript and supplemental information.

Experimental Methods

Materials

Ta-doped LLZO ($\text{Li}_{6.6}\text{La}_3\text{Zr}_{1.6}\text{Ta}_{0.4}\text{O}_{12}$) was obtained from Toshima Corp. The materials were manufactured using a hot press to ensure a high density (>99% relative to theoretical), with an average grain size of 2 μm from our previous study⁹. Elemental composition analysis provided by Toshima indicates that less than 0.01% by weight Fe, Ca, and Cr are present in the material. Lithium-metal foil (purity > 99.9%) was obtained from Alfa Aesar.

Thin-film Deposition

Metallic coatings were deposited through RF sputtering from a 2-inch Titan magnetron sputter source (PVD Products) in PLD/MBE2300 vacuum deposition system (PVD Products) at room temperature. To initiate the plasma, an Ar flow rate of 15 sccm and a pressure of 30 mTorr were applied, subsequently reducing to 5 mTorr during the deposition. The RF power was set at 200 W with an immediate power ramp-up. After each deposition, the samples were post-annealed at various temperature (100-400 °C) for 1 hour in an Ar pressure of 5.0×10^{-7} Torr with a ramping up rate of 20 °C/min and a ramping down rate of 50 °C/min. Sputtering was accomplished using a high-purity Ag target (99.99% purity) from AJA International, Inc. The deposition rate was 3 Å/s.

SEM microprobe electrochemical cell construction

The microprobe system consisted of a Kleindiek MM3A manipulator and a Ted Pella tungsten microprobe (Autoprobe 100 & 200, taper angle of 10°). The detailed instructions for building a cleaved LLZO cell for *operando* SEM has been reported in our previous study⁹: the tungsten probe served as the working electrode, and the lithium-metal foil (200-300 μm thick after purification at 200°C) functioned as the counter electrode in a two-electrode cell configuration. To electroplate lithium metal, we performed linear sweep voltammetry experiments starting at 0 V vs. Li/Li⁺ and at a constant sweep rate of -5 mV/s. The tungsten probe was shaped at 30 kV using the Ga⁺ FIB system to achieve a truncated cone with the terminal end attaining a contact diameter of ~1.5 μm for a landing force of 5 mN, resulting in contact pressure of ~3 GPa. The force remained throughout the Li electroplating experiments. In contrast, for surface electronic conductivity study, a minimal contact pressure of less than 100 MPa applied, employing a loading force of <0.05 mN at a contact diameter of ~0.8 μm. The probe loading force on LLZO surface was measured by a spring table (Kleindiek, spring constant 1000 N/m).

Characterization

Optical images of LLZO samples were taken using a Keyence VHX-7000 digital microscope *via* reflective white light depth composition imaging.

NanoSIMS characterization was conducted using Cameca NanoSIMS 50L on an area of 30×30 μm. Isotopes including ⁷Li, ⁹⁰Zr, ¹⁰⁹Ag were studied. Operation beam current FCo of 10 pA was used by selecting aperture of D1-3, slits of ES-2 and AS-1. ¹⁰⁹Ag is selected for mass resolving power (MRP) optimization achieving a high MRP of ~4900. The sample was transferred to a

loadlock chamber *via* a customized portable glovebox flowing with Ar gas (99.99% purity) prior to sample loading to minimize air contamination on LLZO. No pre-sputtering is performed before each analysis. Sputtering rate by Cs⁺ source is calibrated as 0.42 ± 0.06 nm per each scan ($t = 1.1$ min) on LLZO at beam current of 10 pA with calibration method elaborated in Figure S20.

X-ray photoelectron spectroscopy (XPS) was collected with PHI VersaProbe 3 XPS with an Al K-alpha source (1486 eV). The LLZO sample was transferred from the Ar-filled glovebox to the XPS in a vacuum transfer vessel to prevent air exposure. The depth profiles were collected using Ar⁺ sputtering (1 kV, 0.7 μA, 2 x 2 mm). Both electron and ion neutralization sources were used in data collection. In the energy calibration process, we used the initial scan's metallic state of Ag 3d_{5/2} at 368.3 eV as the reference point for calibrating all the peaks of Ag 3d, Zr 3d, and La 3d. As the depth profile scans progressed, we aligned each Zr 3d peak in every scan to the Zr 3d peak at the final scan to calibrate all peaks. This approach aimed to minimize any peak shifting during Ar⁺ sputtering, although the actual shifting observed was minimal (<0.1 eV). Notably, the XPS depth profiles of Ag 3d, Zr 3d, and La 3d without aligning Zr 3d peaks (Figure S3) showed negligible shifting and yielded identical results to those in Figure 1c.

Nanoindentation: mechanical characterization of LLZO was conducted using an *in-situ* SEM nanoindenter (NanoFlip, KLA) to protect the sample from air contamination during testing. The nanoindentation was performed at a constant strain rate of 0.2/s up to 50 mN using a cube corner tip. Fracture force was measured based on the first “pop-in” event that is greater than 10 nm in the load-displacement curve. 29 and 40 samples were examined on uncoated and Ag⁺-LLZO, respectively. Internal consistency of the 69 tests was confirmed by calculating the elastic

modulus based on the unloading curve of each test, described in Figure S21. Hertzian contact stress was calculated using the following equation:

$$F = \frac{4}{3} E_r R^{\frac{1}{2}} d^{\frac{3}{2}},$$

where R is the measured tip radius of 65 nm, d is the depth, E_r is the reduced elastic modulus determined as follows:

$$\frac{1}{E_r} = \frac{1 - \nu_{LLZO}^2}{E_{LLZO}} + \frac{1 - \nu_{diamond}^2}{E_{diamond}}$$

where $\nu_{LLZO} = 0.24$ for Poisson's ratio of LLZO, $E_{LLZO} = 150$ GPa for LLZO⁴⁷, $\nu_{diamond} = 0.07$ for Poisson's ratio of the diamond tip, $E_{diamond} = 1141$ GPa for the elastic modulus of the diamond.

(S)TEM: LLZO lamellae for (S)TEM were prepared by FEI Helios NanoLab 600i DualBeam with final polishing at 5kV Ga⁺ beam with a Pt capping layer (200 nm from electron beam induced deposition followed by ~1.5 μm from Ga⁺ beam induced deposition) to protect the surface from Ga⁺ beam damage. Then lamellae were transferred to cryogenic dewar and immersed in liquid nitrogen to avoid air reactivity before loading to (S)TEM. For cryo-EM characterization, the lamellae, while still immersed in liquid nitrogen, were loaded into the Gatan side-entry cryo-transfer holder (Gatan model 626), which was then inserted into the (S)TEM column. To maintain the specimen in its native state, a specialized cryo-shutter was employed within the cryo-EM holder, preventing air exposure and ice condensation onto the sample. Once inside the TEM column, the temperature was maintained at approximately -174 °C to achieve the cryogenic conditions required to minimize beam damage during operation. Cryo-EM

experiments were conducted on a ThermoFisher Titan 80-300 environmental (scanning) transmission electron microscope operated at an accelerating voltage of 300 kV using bright field (BF), high-resolution transmission microscopy (HRTEM), and high-angle annular dark-field (HAADF) imaging modes. The instrument was equipped with an aberration corrector in the image-forming lens, which was calibrated before each sample analysis. Cryo-STEM EELS characterization was performed with a C2 aperture of 50 nm, a probe current of 200 pA, a camera length of 38 mm, a pixel dwell time of 20-100 ms, and a pixel size of 3 nm. EELS spectra were acquired on a high-resolution Gatan imaging filter (GIF Quantum 966) with a dispersion of 0.25 eV/channel in Dual EELS mode, with the low-loss spectrum centered on the Li K-edge and the core-loss spectrum centered on the Ag M-edge. Maps were computed through a two-window method, with a pre-edge window of 20-40 eV fitted to a power-law background and a post-edge window of the same width on the core-loss signal.

Computational Methods

Density Functional Theory

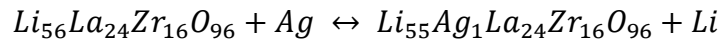
A $1 \times 1 \times 1$ cell was chosen for LLZO. The structure chosen was the cubic (Ia-3d) phase with lattice constant 13.003 Å. The Li⁺ filling rules were as defined in^{48,49}. The Li₂O (Fm-3m), Li (Im-3m) and Ag (Fm-3m) structures were obtained from Materials Project⁵⁰.

All Density Functional Theory (DFT) calculations were carried out using the Vienna Ab Initio Simulation Package (VASP)⁵¹. The plane wave basis set was chosen with the energy cutoff set to 600 eV. The electronic interaction between the core and electrons was modeled using the projected plane waves (PAW) method. The electronic exchange correlation functional used the

generalized gradient approximation (GGA) by Perdew, Burke and Ernzerhof (PBE)⁵². For the electronic relaxation, the energy criterion was set to 10^{-5} eV and a Gaussian smearing width of 0.1 eV was used. For ionic minimization, the force criterion was set to 0.03 eV/Å. A $1\times 1\times 1$ Monkhorst Pack K point mesh chosen was chosen.

To obtain the structure for ion exchanged Ag⁺-LLZO ($\text{Li}_{55}\text{Ag}_1\text{La}_{24}\text{Zr}_{16}\text{O}_{12}$) one Li⁺ in $\text{Li}_{56}\text{La}_{24}\text{Zr}_{16}\text{O}_{12}$ was exchanged with one Ag⁺ (corresponding to ~1.7% exchange) in the simulation box. A total of 21 distinct Li⁺ were chosen (14 from Octahedral, 7 from Tetrahedral) for exchange. A full relaxation was performed for each case and the lowest energy configuration was chosen for all further DFT calculations.

For Ag-Li ion exchange, the reaction is

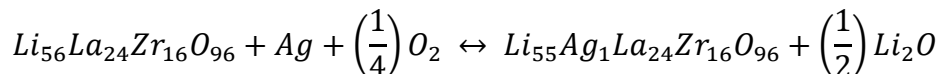


and

$$E_f(0K) = E_{IX} - E_{LLZO} + E_{Li} - E_{Ag}$$

E_{IX} , E_{LLZO} refer to the DFT computed energies of the ion-exchanged LLZO, pristine LLZO respectively and E_{Li} and E_{Ag} refer to metallic Li and Ag.

For the reaction with the residual oxygen



$$E_f(0K) = E_{IX} - E_{LLZO} - E_{Ag} - \frac{1}{4}E_{O_2} + \frac{1}{2}E_{Li_2O}$$

Where E_{O_2} is the DFT energy of an isolated O₂ molecule in a cubic box of 20×20×20 Å³ with a bond length of 1.23 Å⁵³ and E_{Li_2O} is the DFT energy of Li₂O.